

Influence of in-plane and out-of-plane stiffness on the stability of free-edge gridshells: A parametric analysis

Original

Influence of in-plane and out-of-plane stiffness on the stability of free-edge gridshells: A parametric analysis / Venuti, Fiammetta; Bruno, Luca. - In: THIN-WALLED STRUCTURES. - ISSN 0263-8231. - ELETTRONICO. - 131:(2018), pp. 755-768. [10.1016/j.tws.2018.07.019]

Availability:

This version is available at: 11583/2712019 since: 2018-08-28T08:35:18Z

Publisher:

Elsevier Ltd

Published

DOI:10.1016/j.tws.2018.07.019

Terms of use:

This article is made available under terms and conditions as specified in the corresponding bibliographic description in the repository

Publisher copyright

Elsevier postprint/Author's Accepted Manuscript

© 2018. This manuscript version is made available under the CC-BY-NC-ND 4.0 license
<http://creativecommons.org/licenses/by-nc-nd/4.0/>. The final authenticated version is available online at:
<http://dx.doi.org/10.1016/j.tws.2018.07.019>

(Article begins on next page)

Influence of in-plane and out-of-plane stiffness on the stability of free-edge gridshells: a parametric analysis

Fiammetta Venuti^{a,*}, Luca Bruno^a

^aPolitecnico di Torino, Department of Architecture and Design,
Viale Mattioli 39, I-10125, Torino, Italy

Abstract

Gridshells are form-resistant structures, which are suitable for covering large spans, especially when lightness and transparency are respectively relevant architectural and functional requirements. The majority of built gridshells are characterised by one or more free-edges, which derive from trimming the gridshell reference surface in order to provide building access or to integrate the gridshell within existing structures. Up to now, only few scientific systematic studies have been devoted to the effects of elastic boundary structures on the stability of gridshells. This study aims at filling some gaps about this issue. To do so, an ideal free-edge bending-inactive hybrid single-layer gridshell is analysed. The gridshell sensitivity to the flexural stiffness of the boundary arch and to the shear stiffness of the gridshell are investigated through an extensive parametric analysis, which was performed by means of numerical experiments. Results are first discussed in terms of the well-established load factor and buckling shape. Then a complementary mechanical reading is provided by introducing ad-hoc conceived local metrics of the in-plane and out-of-plane deformations at collapse. Three different mechanical regimes at collapse are outlined. In conclusion, a range-finding chart within the design parameter space is proposed to orient the structural analyst in the choice of the preferred regime.

Keywords: hybrid single-layer gridshell, instability, free-edge, boundary stiffness, numerical experiments

Nomenclature

GMNA	Geometrically and Materially Nonlinear Analysis
LBA	Linear Buckling Analysis
LF	Load Factor
CG	Complete Gridshell
PG	Partial Gridshell
E	modulus of elasticity
L	dome span length
f	dome rise length
l	characteristic length of quadrilateral face
p	subscript of the generic structural node
P	number of structural nodes
x	horizontal space coordinate
y	horizontal space coordinate
z	vertical space coordinate
K	discrete gaussian curvature
\mathbf{K}_e	elastic stiffness matrix

*Corresponding author. Tel: (+39) 011-090.4862
Email address: fiammetta.venuti@polito.it (Fiammetta Venuti)

\mathbf{K}_g	geometric stiffness matrix
I_b	moment of inertia of the boundary structure
I_e	moment of inertia of the grid elements
I_r	ratio of the boundary to grid moments of inertia
S_r	non-dimensional ratio between design parameters
Q	nodal resultant load
q	uniform load
s	uniform live (snow) load
g	dead load
A	quadrilateral surface
A_e	cross section area of grid elements
A_c	cross section area of diagonal cables
f_y	yield strength
ΔK	out-of-plane nodal deformation
γ_{xy}, γ_{yx}	components of the in-plane nodal deformation
Γ	in-plane nodal deformation
ν	nodal direction
μ	load multiplier
σ_0	cable initial prestressing
σ	stress field
ϕ	buckling mode shape
φ	generic buckling shape
λ	eigenvalue
δ	nodal displacement
δ_u	ultimate nodal displacement
κ	cotangent of the nodal angle

1. Introduction

Gridshells are form-resistant structures, which are designed to ideally bear the loads by means of in-plane internal forces. Their geometry is generally defined, at least in steel gridshells, by approximating a reference continuous surface through a discrete pattern of line-like structural members, which are mainly subjected to axial forces.

Gridshells find their natural application in large-span buildings, such as stadia, courtyards and expo pavilions, where transparency and lightness might be relevant program requirements. Not surprisingly, the first known pioneering application of a doubly-curved gridshell, which dates back to the late 19th century and was designed by engineer Vladimir Shukov, refers to the roof of a large-span Plate Rolling Workshop in Russia [1]. The geodesic dome of the Zeiss-Planetarium in Germany, designed by Walther Bauersfeld and completed in 1926, is another example of this kind. Throughout the second half of the 20th century, the milestone achievements of Buckminster Fuller [2], Frei Otto [3] and Schlaich Bergermann und Partner [4, 5] helped defining the current technology and strategies for gridshell design: on the one hand, the work of Frei Otto gave birth to what is currently known as a bending-active, or post-formed, timber gridshell [6, 7]; on the other hand, Jörg Schlaich and Hans Schober focused on bending-inactive, or pre-formed, steel/glass gridshells, most of which were derived from surfaces of translation and were based on the use of quad patterns [8]. Since these pioneering structures, the gridshell structural concept has been widely applied to a variety of buildings all over the world, both in traditional materials [5, 9] and innovative ones [10, 11, 12].

Gridshells are optimised and highly efficient structures, but this efficiency makes them highly prone to buckling phenomena, which can lead to catastrophic collapse. Since the collapse of the Bucharest Exhibition Hall dome in 1963, a lot of research has been devoted to buckling and post-buckling behaviour of reticulated shells [13, 14, 15, 16, 17, 18, 19, 20]. The first approach to the problem was based on the continuum analogy, that is, the behaviour of the gridshell is compared to the one of a shell, characterised by the same geometry of the gridshell and by an equivalent thickness [21, 22, 23, 24]. The aim of this approach was to extend to gridshells the analytical expressions of the buckling load that were available for continuous shells. This method, even though it can be useful in a preliminary

design phase, presents some drawbacks [13]: analytical solutions are available only for a class of continuous shells, characterised by specific shape and boundary conditions; the continuum analogy does not allow to account for some types of buckling that are peculiar of gridshell structures, such as nodal buckling and member buckling; the influence of joint deformation cannot be taken into account. For all these reasons, the buckling behaviour of gridshells is usually studied by means of non-linear numerical analyses of Finite Element Models of the whole structure.

The main factors, which influence the buckling behaviour of gridshells and that have been studied in the literature, are the following: [13, 25]: i. *the Gaussian curvature* of the gridshell underlying surface [e.g. 13, 26, 16, 19]; ii. *the grid topology and spacing* [e.g. 27, 24, 20, 25]; iii. *the geometrical and mechanical imperfections* [e.g. 28, 29, 26, 30, 31, 32]; iv. *the joint stiffness* [e.g. 33, 29, 16, 34, 35]; v. *the boundary conditions*.

While the effects of the first four factors have been widely studied in the recent past, the last factor has been less explored. Stability studies on gridshell domes are usually carried out by referring to a horizontal spring-plane and rigid supports [29, 26, 15, 27, 36, 18, 37, 24, 38, 20, 39]. The effects of different rigid supports (pinned, roller or fixed) have been comparatively studied in a few papers [40, 41, 13, 19]. Analogously, the gridshell barrel vaults studied in the literature are usually delimited by a horizontal spring-plan and gable vertical plans, which are orthogonal to their axes [26, 19, 39] and rigidly constrained at the spring-lines. To the authors' knowledge, the effects of different rigid supports (fixed or pinned) along the spring-lines of a gridshell barrel vault have been discussed in [19] and [42] only.

Even fewer scientific systematic studies have been devoted up to now to the effects of elastic boundary structures along the delimitation edges on the stability of gridshells, as recently highlighted in [42]: "This kind of elastic boundary has not been extensively investigated, and studies are needed in each design to know how and if the supports improve the buckling resistance.". This is even more surprising knowing that a horizontal spring line and/or infinitely stiff perfect constraints only seldom occur in built gridshells. Usually and more and more frequently, gridshells are trimmed by vertical or inclined planes (e.g. the Shukov gridshell in Vyksa [1]), or by curved surfaces (e.g. the Hippo House at the Berlin Zoo [43]). As a consequence, they are constrained by elastic boundary structures along the delimitation edges. Master builders were certainly aware of the influence of elastic boundaries, as demonstrated by the above cited built structures. However, to the authors' best knowledge, systematic studies applied to double curvature single-layer gridshells are not available, and only a few number of studies analysed the effects of the stiffness of gable boundary structures in barrel vault gridshells. Bulenda and Knippers [26] compared the barrel vault stability with no stiffening boundary arches with the same structure stiffened by a boundary arch having 40 times the stiffness of a IPE 360 profile. As expected, the differences in terms of mechanical behaviour are striking: the unstiffened vault buckles analogously to a plane arch, while a spatial behaviour at collapse takes place in the stiffened vault, even if the stiffening arch still shows not negligible ultimate displacements. Cai et al. [19] stiffen the vault with pre-tensioned spoked wheels transverse diaphragms, analogously to the stiffening system adopted for the roof of the Museum of Hamburg History courtyard [4]. In this case, the arch acts as a perfectly rigid support in its vertical plane.

This issue seems to be disregarded also in the case of continuous shells. A number of remarkable free-edge concrete shells were conceived by master builders such as Heinz Isler [44] and Felix Candela [45]. In their works several solutions were put in place at the shell free boundaries, ranging from unstiffened edge, to creases introducing form stiffness, to edge beams providing inertial stiffness. However, once again "the stability of shells with free edges is a rather unexplored field" [46]. In fact, even though single curvature cylindrical shells with flexible bottom have been widely systematically studied over the past fifty years, and their buckling behaviour is well known [47, 48, 49, 50, 51], analytical solutions for double curvature shells with elastic boundaries are not available in literature.

In summary, a scatter exists between the design practice and the scientific literature in this field. In this framework, the paper focuses on the delimitation of gridshells, and aims to fill in some of the gaps, which are currently evident in the topic literature review. In terms of paper outline, Section 2 defines, classifies and reviews some relevant examples of free-edge gridshells, both from the geometrical and mechanical points of view. The term Partial Gridshells (PG) will be introduced here to denote free-edge gridshells as opposed to Complete Gridshells (CG). A new parametric study is described in Section 3, in terms of geometrical setup, structural setup and design parameter space. Section 4 briefly recalls gridshell structural modelling and computational approaches. The observables selected for post processing are described in Section 5. Results and findings of the parametric analyses are described and discussed in Section 6, in parallel with a resulting range-finding chart, developed in the design parameter space. Section 7 summarises the conclusions and future works.

2. Partial Gridshells: definition and classification

Distinction between Complete Gridshells (CG) and Partial Gridshells (PG) is proposed in this paper. *Complete Gridshell* (CG) refers to gridshells whose shape results from trimming a reference gridshell geometry by a single surface, usually a horizontal or inclined plane. The structure spring lines, along which the gridshell is rigidly constrained, are given by the intersection between the reference geometry and the trimming surface (Figure 1a, red curve). By exclusion, *Partial Gridshell* (PG) denotes gridshell forms which are obtained through two or more geometrical cuts. PGs can be cut by vertical or inclined planes (Figure 1b) or curved surfaces (Figure 1c). PGs spring lines are given by the intersection between the reference geometry and one of the trimming surfaces - usually the one that lies horizontally. The intersection between the reference surface and the other trimming surfaces determines a number of PG free edges (blue dash-dot curves), which are not rigidly constrained.

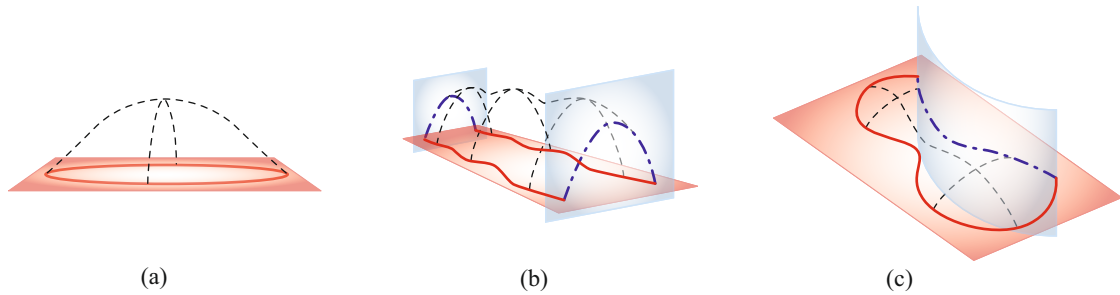


Figure 1: Reference and trimming surfaces of (a) a CG (after the Essen gridshell), (b) a PG cut by vertical planes (after the Downland gridshell) and (c) a PG cut by a curved surface (after the Hippo House)

CGs represent a minority and are mainly applicable when the structure spring lines are raised from the ground level or from extremely stiff substructures. To our knowledge, the only built projects of CG whose spring line lays on the ground level are two research pavilions: the timber bending-active Essen gridshell designed by Frei Otto in 1962 [3] (Figure 2a) and the experimental GFRP bending-active gridshell built at ENPC [52]. However, these prototypes did not have to deal with functionality issues and program requirements. Otherwise, other stiff structural elements are required and introduced to provide building access. The National Maritime Museum in Amsterdam, the Dresden Castle gridshell [53], the Neckarsulm dome [4], the Orangery gridshell at Chiddingstone Castle (Figure 2b), and the roof of the Great Court of the British Museum [54] are outstanding examples of this kind.

PGs include the majority of the built gridshells. In most cases the gridshell form needs to be trimmed due to functional or architectural requirements. When the gridshell spring lines lie on the ground level, the most common issue is to provide openings for building access, as in the Multihalle in Mannheim [55] (Figure 2c), the “Future of us” gridshell pavilion in Singapore [56] (Figure 2d) or the “Ephemeral cathedral” in Paris [10]. When the main gridshell function is to provide shelter, cuts might be necessary for other reasons: for instance, to array the base gridshell geometry, such as in the roof of the production hall in Vyksa [1] (Figure 2e) or in the West entrance of the Hannover Fair [57] (Figure 2f). In both cases, the roof is made of a modular repetition of the same base gridshell, which is trimmed by four vertical planes and, hence, bounded by as many parabolic arches. In other cases, the cuts are made to integrate the gridshell within existing buildings. Typical examples are gridshell roofs over courtyards, streets or squares: two outstanding examples are the Schlüterhof Roof at the German Historical Museum in Berlin (Figure 2g) and the Cabot Circus in Bristol [58] (Figure 2h). Besides functional needs, cuts can also identify architectural gestures, such as in the Hippo House at the Berlin Zoo [43] (Figure 2j) or in the Yas Island Marina Hotel in Abu Dhabi, UAE [59] (Figure 2k). Note that contemporary PGs are delimited by increasingly complex surfaces: vertical single-curvature concave ones (Figure 2j), combinations of planes and surfaces (Figure 2h), double-curvature surfaces (Figure 2k).

The CG mechanical behaviour under uniform loads mainly involves membrane stiffness. The same is expected not to hold for PGs. The structural design of PGs raises further issues with respect to CGs. Specifically, the mechanical behaviour of PGs is expected to be highly dependent on:

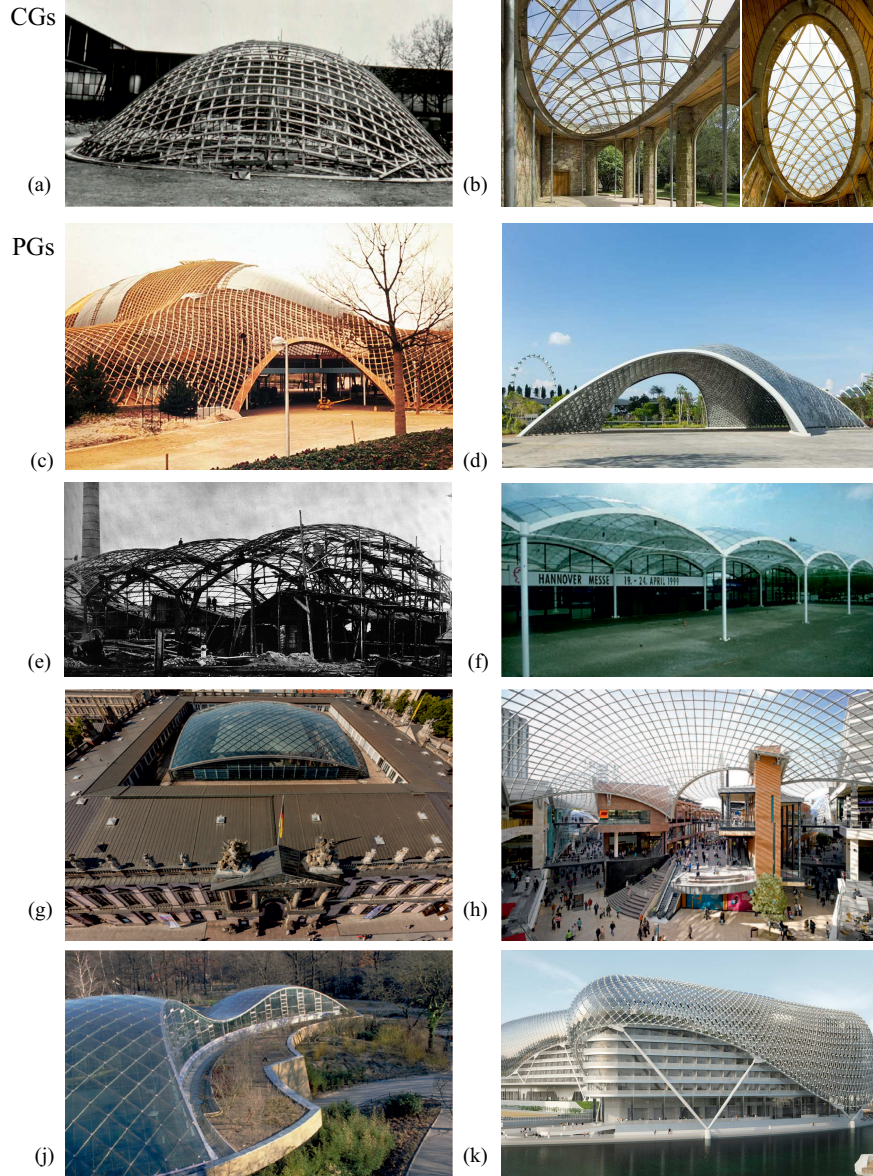


Figure 2: Survey of built CGs and PGs: (a) Essen gridshell [3], (b) Orangery gridshell, (c) Mannheim Multihalle [55], (d) “Future of us” Pavilion [56] (e) Vyksa gridshell [1], (f) Hannover Fair, West entrance [57], (g) Schlüterhof Roof (h) Cabot Circus [58] (i) Hippo House [43], (k) Yas Island Marina Hotel [59]

- *Geometrical factors*: the kind (either planar or curved) of the trimming surface, its orientation with respect to the grid direction, and the ratio between the gridshell and free-edge span (i.e. the location of the trimming surface);
- *Mechanical factors*: the stiffness of the boundaries and the in-plane shear stiffness of the gridshell.

This study focuses on the mechanical factors, while the influence of geometrical factors will be investigated in a subsequent work. The stiffness of the boundaries depends on the cross section of the boundary structure, its length and its constraints. A conceptual categorisation corresponding to increasing degree of stiffening can be outlined:

- the PG edges are not stiffened, that is, the boundaries are free and made of structural elements with the same

cross section as the grid elements. Examples of this kind are the Toledo I gridshell [60], a pavilion for the Naples School of Architecture courtyard, and the Waitomo Caves Visitor Centre [61];

- the PG edges are stiffened by a *boundary structure*, whose axis coincides with the edge curve, and whose flexural stiffness is greater than the flexural stiffness of the grid elements (e.g., boundary arches). The Mannheim Multihalle [55] and Downland Museum [62] are examples of this kind;
- the PG boundary structures are further supported by vertical elements, such as columns, which reduce the length of the free edge. The Hippo House [43] and the Savill Garden gridshell [63] are representative of this category.

The in-plane shear stiffness of the gridshell is mainly related to the kind of adopted mesh pattern. Generally speaking, quad meshes have lower in-plane shear stiffness than triangular meshes. For this reason, quad meshes are often stiffened by bracing cables [4], which have the effect of triangularizing the quad mesh. In this scenario, the cross section of the diagonal elements is the structural parameter that mostly affects the in-plane shear stiffness of the gridshell.

Here, a rough attempt is made to indirectly estimate some reference values of the boundary stiffness and gridshell in-plane shear stiffness of built PGs. Due to the lack of published data, the direct estimation of the stiffness is not affordable in this study. Information about the section geometrical and material properties of the main structural elements can be found more easily in the literature. Figure 3 collects the section properties of the boundary and diagonal elements for a small ensemble of built PGs, whose data were available. The survey includes different gridshell layouts: unbraced and braced quad meshes, triangular meshes, bending-active and inactive, single and double-layer. The selected section properties are the moment of inertia I_b of the boundary elements and the area A_c of the diagonal elements, since they significantly contribute to the boundary stiffness and in-plane shear stiffness of the gridshell, respectively. Both properties are expressed in dimensionless form, by scaling their value with respect to the corresponding quantity of the grid element section:

$$\begin{aligned} I_r &= n I_b / I_e, \\ A_r &= n A_c / A_e \end{aligned} \quad (1)$$

where I_e and A_e are the moment of inertia and area of the grid elements, respectively, and n is the homogenization coefficient given by the ratio between the moduli of elasticity of the boundary/diagonal element material and the grid element material, if materials differ.

Overall, I_r varies in the range [1, 500], where the unit value refers to unstiffened boundary, and A_r in the range [0, 0.5], where $A_r = 0$ refers to the unbraced case. In particular, hybrid bending-inactive single-layer steel gridshells lie in a smaller interval of parameter values i.e. $0 < A_r < 0.1$, and $80 < I_r < 300$. Bending-active timber double-layer gridshells have larger A_r values, i.e. $0.3 < A_r < 0.5$, since they are usually characterised by diagonal elements inbetween the two laths, with the same cross section as the main grid elements in each lath. The Mannheim Multihalle gridshell ($A_r \approx 0.3$) shows some differences among the collected cases, because the steel bracing cables spans over about six gridshell quadrangles made of wood elements.

3. Parametric analysis set-up

The effects of the boundary stiffness and gridshell in-plane shear stiffness on the gridshell stability are investigated through a parametric analysis by computational simulations.

A complete bending-inactive hybrid single-layer gridshell by Schlaich and Schober [4] is used as a reference to derive the studied PG. This gridshell type is chosen because it permits to derive two limit cases: a quadrilateral gridshell, where bracing cables are missing, and a triangular gridshell, in which the cables are replaced by trusses that share the same cross section of the grid elements.

The features of the case study are detailed below.

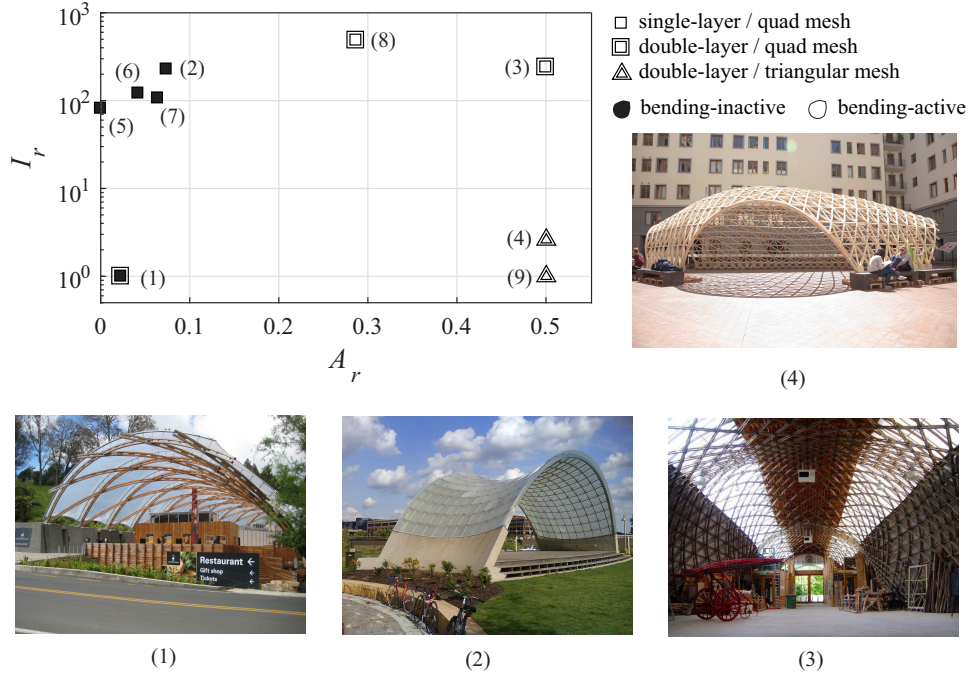


Figure 3: Survey of I_r - A_r values: (1) Waitomo Caves visitor centre [61], (2) Schubert Club Band Shell [64], (3) Downland Museum [62], (4) Toledo I gridshell (photocredit Gianluca Jodice) [60], (5) Cabot Circus [58], (6) courtyard roof at the Engineering Faculty at the University of Pisa [65], (7) Hippo House [43], (8) Mannheim Multihalle [55], (9) Toledo II gridshell [66].

3.1. Geometrical set-up

The geometry of the investigated partial single-layer gridshell is shown in Figure 4. The analytical form of the reference continuous dome (Fig. 4a) belongs to the translational surface type, having a parabola as both the directrix and generatrix, i.e. it is a paraboloid. The considered partial dome is obtained by sectioning the complete dome with a vertical plane corresponding to the $x-z$ plane. The obtained half dome is, therefore, bounded by a vertical parabolic arch, whose geometrical parameters are: span length $L = 30$ m, span to rise ratio $L/f = 8$ (Fig. 4d).

The discrete gridshell geometry results from the point wise sampling of the dome surface in P structural nodes ($p = 1, P$) along the directions of the directrix and generatrix having coordinates $\mathbf{X}(p) = \{x_p, y_p, z_p\}$. The nodes are connected along the directions of the directrix and generatrix by straight segments resulting in elemental planar quads [57], having a characteristic length $l \approx 1.5$ m (Fig. 4b). Each quad is braced by two diagonal cables, as shown in Figure 4c.

3.2. Structural set-up

The grid of quads is composed of steel beams. These are diagonally braced by prestressed cables. The structures are covered with glass panels, which do not contribute structurally but are taken into account as dead loads.

The structure is modelled by means of finite element software ANSYS® v17.2. Both the grid elements and the boundary arch are modelled in ANSYS using the BEAM188 finite element. The grid beam cross section mimics the one usually adopted by [4, 26]: a solid quadrilateral cross section with area $A_e = 2.5e - 3$ m² and moment of inertia $I_e = 5.2e - 7$ m⁴ is chosen. The 3D beam elements are based on Timoshenko's beam theory and adopts a cubic shape function. The cables are modelled by 3D tension-only trusses with circular cross section (LINK180 finite element in ANSYS).

The whole structure is assumed to be hinged at the boundaries, while the joints between steel bars are modelled as rigid, as usually done in the literature [26, 37, 27].

The constitutive model of the steel is linear elastic - perfect plastic, with a yield strength equal to $f_y = 355$ MPa, Young's modulus $E = 2.1e + 5$ MPa and Poisson's ratio $\nu = 0.3$. The diagonal cable prestressing is equal to $\sigma_0 = 100$

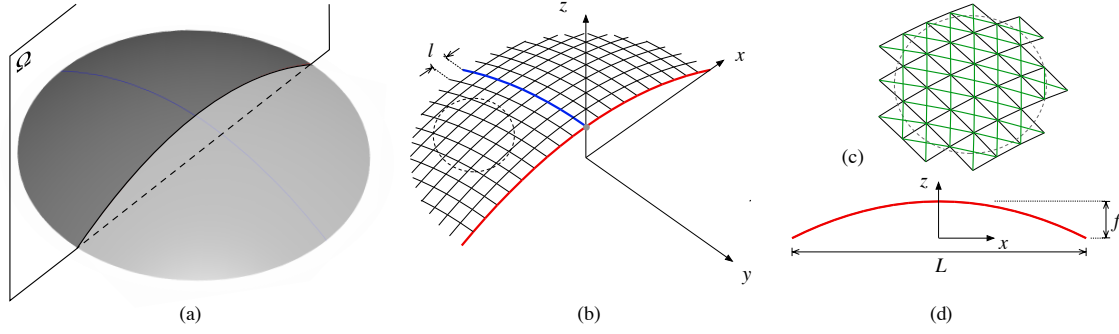


Figure 4: Set-up geometry: reference continuous surface (a), discrete gridshell surface (b, shown without cables), close-up view of a part of the dome including diagonal cables (c), section along the meridian vertical plane (d)

MPa, while steel bars are not subject to initial bending. The dead load g of structural steel members and of 20 mm-thick glass glazing is set equal to 0.5 kN/m^2 . As for the live load s , a uniform snow load $s = 0.75 \text{ kN/m}^2$ is applied on the structure. A uniform load case $q = 1.3g + 1.5s$ is applied to the structure. The resultant p -th nodal load is defined as $Q_p = \int_A q da \approx 4000 \text{ N}$, being A the quad surface.

3.3. Parametric analysis plan

For the adopted and fixed geometrical and structural set-ups, the boundary arch stiffness and the gridshell in-plane shear stiffness only depend on two design parameters, namely I_r and A_r , defined according to Eq.s (1). I_b is set equal for both the local axes of the arch cross section. Hence, it affects both the in-plane and out-of-plane flexural stiffness of the boundary arch. A_c affects the axial stiffness of the cables and therefore provides additional in-plane shear stiffness to the gridshell faces, with respect to the unbraced case. As a preliminary remark, it is worth noting that the out-of-plane behaviour of the boundary arch not only depends on its flexural stiffness, but also on the in-plane shear stiffness of the gridshell. This holds also when I_b tends to infinity and the arch behaves as a rigid body, being the arch hinged at its external boundaries. We also point out that the parameter I_b is expected to locally affect the stiffness of the gridshell boundary, while A_c uniformly affects the stiffness of the whole gridshell.

I_r varies in the range $[1, 10^6]$, where the lower and upper values correspond to unstiffened and infinitely stiffened boundary structure, respectively. A_r varies in the range $[0, 1]$. The lower bound corresponds to the limit case of unbraced quad gridshell, while the upper bound corresponds to the limit case where the cable cross section equals the grid element one. The boundary regions of the parametric analysis plan are not necessarily of practical interest in the real world design practice. Nevertheless, the computational testing allows to explore also uncommon, or even unphysical, scenarios to shed some light on the trend of the structural behaviour towards limit conditions.

Figure 5 illustrates the resulting $I_r - A_r$ parameter plan. Besides the limit values above, the values of both parameters are selected in the light of the survey made in Section 2 (Figure 3) for bending-inactive hybrid gridshells. In particular, the parameter space is more densely sampled in the I_r range $[1, 10^3]$ and in the A_r range $[0, 0.1]$, which is the one of design interest for bending-inactive single-layer quad mesh gridshells. In total, 38 values of I_r and 7 values of A_r are explored, resulting in 266 simulations for each kind of structural analysis described in the following Section.

4. Structural modelling

Two kinds of structural analysis are performed and briefly recalled below.

Linear Buckling Analysis (LBA)

LBA solves the eigenvalue problem:

$$[\mathbf{K}_e + \lambda \mathbf{K}_g(\sigma)] \Phi = 0, \quad (2)$$

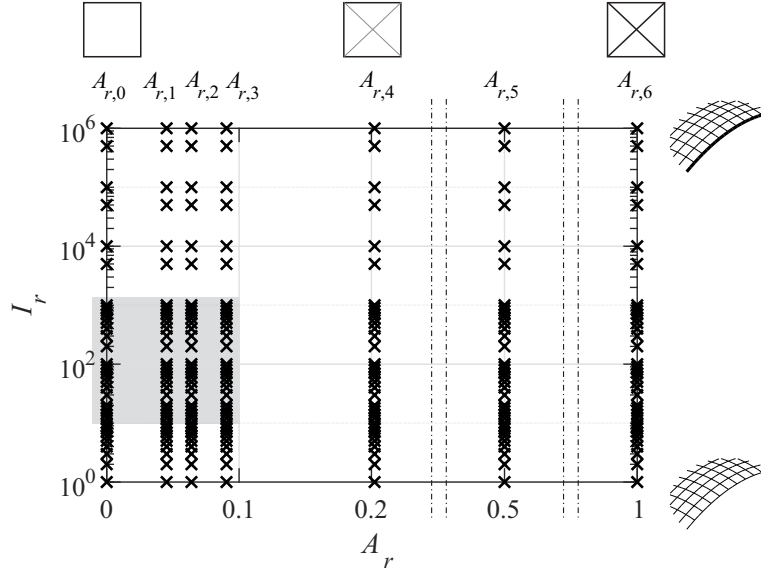


Figure 5: Discretisation of the I_r – A_r parameter plan. The grey area focuses on the values adopted in design practice of bending-inactive single-layer gridshells

where λ is the vector of load factors and Φ is the matrix of the associated buckling mode shapes. The geometric stiffness $\mathbf{K}_g(\sigma)$ is a function of the stress field σ . \mathbf{K}_g is evaluated through a static analysis that solves the equation

$$[\mathbf{K}_e + \mathbf{K}_g(\sigma_0)] \delta = \mathbf{Q} \quad (3)$$

where \mathbf{K}_e is the elastic stiffness, $\mathbf{K}_g(\sigma_0)$ accounts for the initial prestress σ_0 , if any, and \mathbf{Q} is the applied load.

Geometrically and Materially Nonlinear Analysis (GMNA)

$$[\mathbf{K}_e(\delta) + \mathbf{K}_g(\delta)] \delta = \mu \mathbf{Q} \quad (4)$$

where the geometric stiffness $\mathbf{K}_g(\delta)$ is a function of the displacement field $\delta(\sigma)$ and μ is the load multiplier that increases along the simulation. In the study, the steel nonlinear stress-strain relation is modelled by a bi-linear law (elastic-perfect plastic). Due to the progressive yielding of members under monotonically increasing load, the overall structural behaviour is described by a tangent stiffness matrix \mathbf{K}_e which softens for increasing displacement field $\delta(\sigma)$.

Buckling instability of SLGS is highly sensitive to imperfections, that should be taken into account in the structural design of gridshells. Despite this, in the present study both LBA and GMNA are performed on the perfect structure, i.e. neglecting the effects of equivalent nodal imperfections. This choice is due to four reasons: i. the choice of the imperfection shape to adopt in the design is still an object of debate in the civil engineering community [26, 38]; ii. the most popular imperfection models, e.g. [67], assume that the imperfection shape is equal to the first buckling mode shape, that depends in turn on the same parameters of the sensitivity study, i.e. I_r and A_r ; iii. the effects of the imperfection cumulate with, and are expected to prevail on, the parameter primary mechanical effects. It follows that the latter ones are noised and hidden by the former ones; iv. the computational testing, unlike testing on physical models, offers the opportunity to fully control or exclude some parameters and related effects (i.e. nodal imperfections in current case), to focus on the parameters of interest only, to isolate their effects, and finally to discuss results in a clearer and mechanically sound way.

The structural analysis is performed by means of the finite-element code ANSYS® v17.2. The Load Control procedure is applied within GMNA, where the iterative convergence is accomplished at each step by means of the standard Newton Raphson method [68].

5. Definition of the observables

To provide a synthetic description of the mechanical behaviour of the PG versus the selected design parameters, one bulk parameter and two nodal observables are adopted. They are defined in the following with reference to a PG with P structural nodes having coordinates $\mathbf{X}(p) = \{x_p, y_p, z_p\}$ ($p = 1, P$).

5.1. Load Factor (LF)

The load factor is the most relevant parameter usually considered at the Buckling Limit State. Its definition is herein recalled:

$$\mathbf{Q}_u = \text{LF } \mathbf{Q} \quad (5)$$

where \mathbf{Q}_u is the ultimate buckling load and \mathbf{Q} is the load condition as defined in Section 3.2. Within LBA, $\text{LF} = \lambda_1$, i.e. the lowest eigenvalue, which corresponds to the buckling mode shape ϕ_1 . Within GMNA, $\text{LF} = \mu_u$, being μ_u the load multiplier that induces the collapse ($dQ/d\delta = 0$ in a selected reference node), i.e. reaching a limit point, and δ_u the corresponding displacement field.

5.2. Out-of-plane nodal deformation ΔK

In order to locally evaluate the out-of-plane nodal deformation of the gridshell, the following nodal quantity is defined:

$$\Delta K(p) = K(p) - K_0(p), \quad (6)$$

where $K(p)$ and $K_0(p)$ are the discrete gaussian curvatures in the deformed and undeformed shapes, respectively. The discrete gaussian curvature $K(p)$ mimics at each node p the Gaussian curvature in the continuous analogy. With reference to Figure 6, it is defined as [69, 70]:

$$K(p) = 2\pi - \mathcal{E}_p \mathcal{N} - \mathcal{N}_p \mathcal{W} - \mathcal{W}_p \mathcal{S} - \mathcal{S}_p \mathcal{E} \quad (7)$$

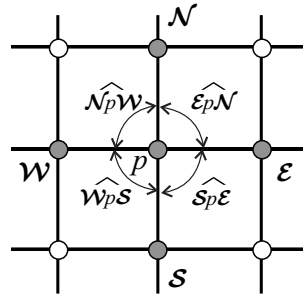


Figure 6: Definition of the discrete gaussian curvature $K(p)$

In the following, $\Delta K = K_u - K_0$ is adopted to mimic in discrete form the variation of the Gaussian curvature of a continuous shell between the undeformed geometry and the collapse deformed shape.

5.3. In-plane nodal deformation Γ

To locally evaluate the in-plane deformation of each quadrilateral face, a nodal quantity equivalent to the shear deformation in continuum mechanics is defined in the following:

$$\Gamma(p) = \gamma_{xy}(p\mathcal{N}) + \gamma_{yx}(p\mathcal{E}), \quad (8)$$

where

$$\gamma_{xy}(p\mathcal{N}) = \frac{|\delta_{x,\mathcal{N}} - \delta_{x,p}|}{l_{p\mathcal{N}}}, \quad \gamma_{yx}(p\mathcal{E}) = \frac{|\delta_{y,\mathcal{E}} - \delta_{y,p}|}{l_{p\mathcal{E}}} \quad (9)$$

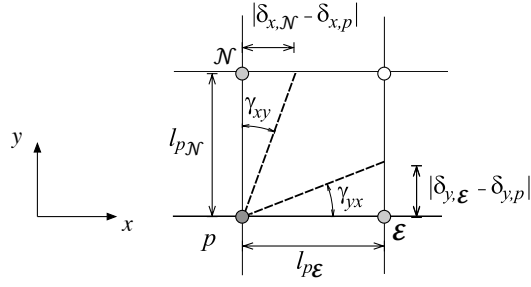


Figure 7: Definition of the equivalent shear deformation $\Gamma(p)$

and the displacement δ , the side of the quadrilateral face l and the node nomenclature are graphically defined in Figure 7 for the sake of clarity and conciseness.

In the following, $\Gamma = \Gamma_u$ refers to the collapse deformed shape, i.e. the displacements δ in Eq. 9 are the ultimate nodal displacements δ_u .

6. Results

This Section illustrates the results of the parametric analysis on the benchmark PG. First, the effects of the design parameters $A_r - I_r$ on Load Factor and buckling shapes are commented in 6.1. Then, the mechanical behaviour is rephrased in 6.2 by introducing a single synthetic design parameter and by referring to nodal observables. Different mechanical regimes are identified. Finally, a range-finding chart within the design parameter plan is presented in 6.3.

6.1. LF and buckling shapes versus design variables

Figures 8(a) and (b) show the LF versus I_r for each A_r obtained by LBA and GMNA, respectively.

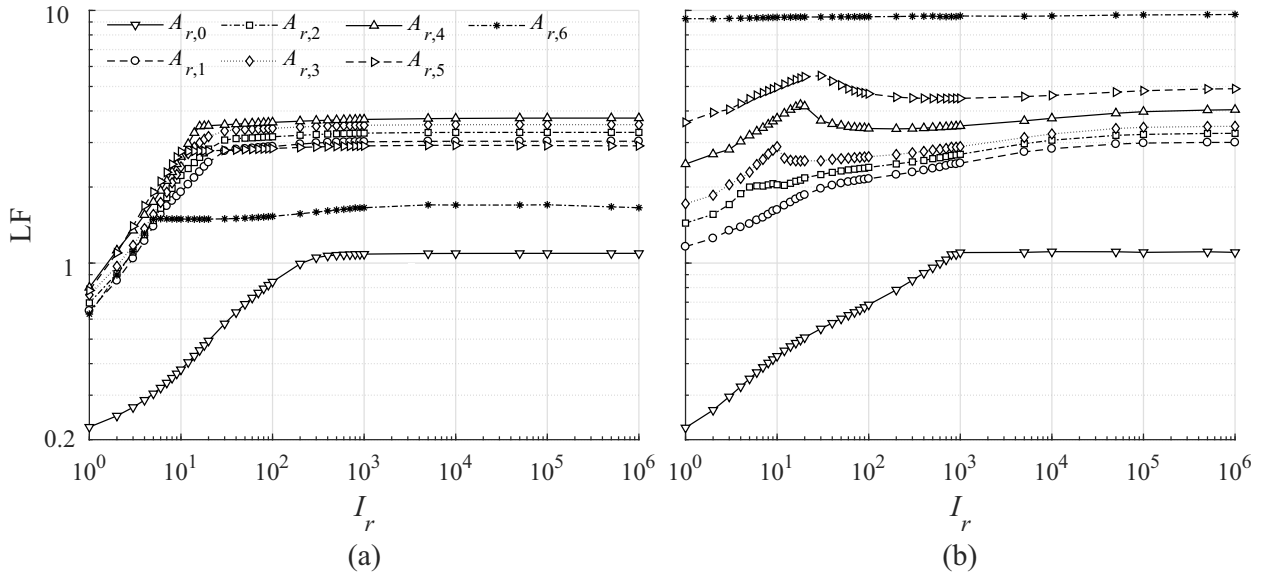


Figure 8: LF versus I_r for different values of A_r with LBA (a) and GMNA (b)

A general trend can be recognised for both kinds of analysis. LF increases for increasing stiffness of the boundary arch along two main branches: a first steeper branch and a second constant or slightly increasing one. However, the

value of I_r at which and the way in which the transition between the two branches occurs differ in the two models and for different values of A_r . In LBA the switch between branches is clearly recognisable, and regularly occurs for decreasing values of I_r as A_r increases. GMNA retains the same trend, and also almost the same LF values, only for the unbraced gridshell ($A_{r,0}$). Conversely, for the other values of A_r , a third branch can be observed in between the first twos. In such a further branch, the LF trend versus I_r is still increasing for $A_{r,1}$, almost constant for $A_{r,2}$, and locally decreasing for $A_{r,3}$ to $A_{r,5}$. Furthermore, the third branch occurs at decreasing values of I_r up to $A_{r,2}$ and at increasing values of I_r from $A_{r,3}$. For $A_{r,6}$ the LF is nearly constant versus I_r .

For low to moderate values of $A_r \leq A_{r,4}$, the LF values predicted by LBA in the first steeper branch are lower than the ones obtained by GMNA, contrarily to what might be expected [42]. At the upper limit of the second constant or slightly increasing branch the two models predict comparable LF values. For high values of $A_r \geq A_{r,5}$, the LFs predicted by GMNA are higher than the ones obtained by LBA whichever the value of I_r . The obtained results show that LF is more sensitive to A_r than to I_r , and suggest that the non linear effects due to bracing cables in hybrid gridshells play a major role, which is necessarily underestimated by LBA.

We can expect that the above differences in LF reflect different simulated modes of instability. Hence the trends of LF can be better commented on by looking at the buckling shapes obtained via LBA and GMNA for some representative values of I_r and A_r (Figure 9). As regards A_r , three values are selected: $A_{r,2}$ is representative of built bending-inactive single-layer steel gridshells (see Figure 3, $A_{r,2} = 0.064$ as for the Hippo House); lower and upper limit cases ($A_{r,0} = 0$, $A_{r,5} = 0.5$) consider the unbraced cell and a very in-plane-rigid gridshell, respectively. The buckling shapes corresponding to $A_{r,6}$ are not plotted because the extreme stiffness of the gridshell involves almost constant values of LF versus I_r in GMNA, and it does not allow a sound kinematic reading of the buckling shapes. As regards I_r , six values are selected: besides the limit values $I_r = 1$ and 10^6 , four other values belong to the above described branches. An overall view of the buckling shapes allows to qualitatively identify some peculiar instability modes:

- the buckling shapes above the red dashed line are characterised by global instability mainly driven by the buckling of the boundary arch:
 - the buckling mode predicted by LBA is asymmetric in most cases, while GMNA always provides symmetric buckling shapes due to the perfect geometry and symmetrical setup. This usually results in an even number n of antinodes in LBA arch buckling shape, and in $n + 1$ antinodes in GMNA;
 - LBA predicts a symmetric arch buckling shape for some pairs of $I_r - A_r$ values (highlighted in grey in Fig. 9). It can be argued this is a consequence of the symmetric elastic constraint that cell bracing provides to the boundary arch. Such a constraint always holds for $A_r > 0$, but its effect depends on the ratio between the free edge bending stiffness and the cable axial stiffness;
 - the stiffening effect of the braced cells on the arch is higher in geometric non linear analysis than in linear analysis, because of the updated overall geometry of the braced cells;
 - in the light of the comments above, the higher LF values by GMNA look mainly due to the additional bracing stiffness accounted for by nonlinear analysis, while the switch from asymmetric to symmetric buckling shapes due to the GMNA symmetric setup seems to play a minor role, as testified by e.g. the minimal scatter of LF from LBA to GMNA for the unbraced PG, $A_{r,0}$;
- the buckling shapes below the blue dash-dot line are still characterised by global instability, but here the buckling mainly occurs on the gridshell, while the arch is almost undeformed. However, the two structural models provide different kinds of instability modes for the braced gridshells:
 - the shell-like buckling mode predicted by LBA involves the majority of nodes with a shorter wavelength than the cases above;
 - GMNA predicts a snap-through buckling of the gridshell portions with the lowest curvature, which are located near the spring line ("line or ring instability" according to the nomenclature in [13]);
- the buckling shapes in between the red and blue lines are characterized by a combined global instability, in which both the arch and the gridshell buckle. This combined instability is more evident for A_r values of design

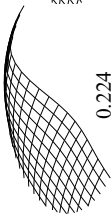
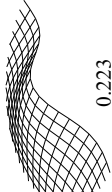
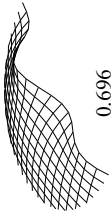
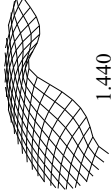
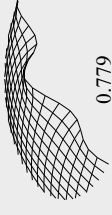
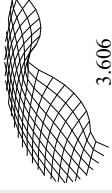
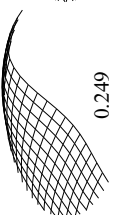
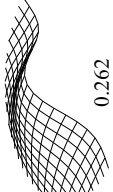
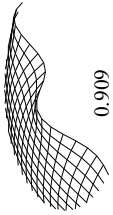
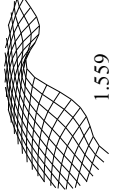
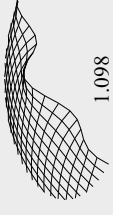

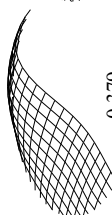
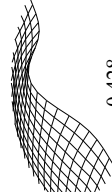
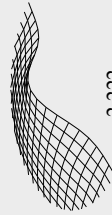
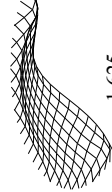
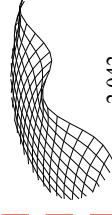
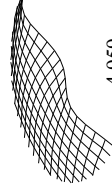



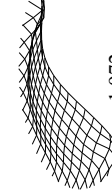

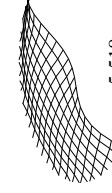
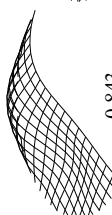


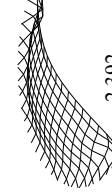

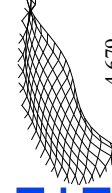
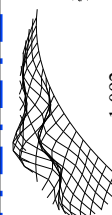
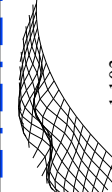

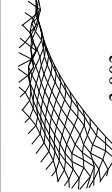

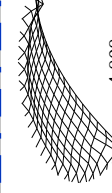
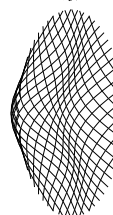
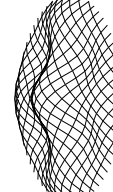

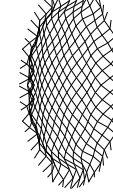
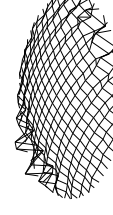
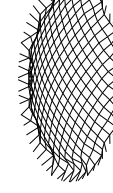
	$A_{r,0}$		$A_{r,2}$		$A_{r,5}$	
	LBA	GMNA	LBA	GMNA	LBA	GMNA
$I_r = 1$	 0.224	 0.223	 0.696	 1.440	 0.779	 3.606
$I_r = 2$	 0.249	 0.262	 0.909	 1.559	 1.098	 3.943
$I_r = 10$	 0.379	 0.428	 2.222	 1.625	 2.042	 4.959
$I_r = 30$	 0.576	 0.550	 3.069	 1.972	 2.240	 5.518
$I_r = 100$	 0.843	 0.684	 3.162	 2.392	 2.842	 4.679
$I_r = 10^6$	 1.092	 1.103	 3.291	 3.003	 2.911	 4.898
CG	 0.690	 0.790	 3.770	 3.951	 3.520	 6.212

Figure 9: Buckling shapes and LF for selected values of I_r and A_r

interest ($A_{r,2}$) than for limit values. The pairs of $I_r - A_r$ in this region generally fall in the third intermediate branch recognized for GMNA in the $LF(I_r)$ curves (Fig. 8).

Some further comments cross the three instability modes outlined above for limit values of A_r . For $A_{r,0}$ the kind of instability predicted by both LBA and GMNA is almost the same for every I_r , except for the asymmetric and symmetric shapes, respectively, induced by the adopted model. This reflects in the close trend of the $LF(I_r)$ curves (Fig 8). For $A_r \geq A_{r,5}$ the bracing stiffening accounted for by GMNA progressively prevails on the flexural stiffness of the boundary arch for every value of I_r . This is the reason why $LF(I_r)$ is slightly varying for $A_{r,5}$ and nearly constant for $A_{r,6}$ in GMNA (Fig 8).

The effect of the cable stiffness on the LF is further investigated in Figure 10 for the limit case $I_r = 10^6$, i.e. extremely stiffen boundary arch (empty triangles). The $LF(A_r)$ trend by LBA (Fig. 10a) and GMNA (Fig. 10b) is qualitatively the same for $A_r \leq A_{r,4}$, i.e. LF increases for increasing A_r . Conversely, for $A_r \geq A_{r,5}$ the bracing stiffening accounted for by GMNA keep the monotonic increasing trend of $LF(A_r)$, while in LBA the shell-like buckling progressively localises, and the LF trend becomes decreasing in turn.

In the case $I_r = 10^6$ the behavior of the PG can be directly compared to the one of the corresponding Complete Gridshell. CG develops along the whole reference dome surface shown in Figure 4(a), it has the same cross section properties, the same internal and external constraints and it is loaded by the same uniform distributed load as the PG. The $LF(A_r)$ for both PG and CG are plotted in Figure 10 by empty and filled triangles, respectively, while buckling shapes of the CG for some selected values of A_r are included in Figure 9, last row. For all values of A_r , the bending stiffness of the boundary arch in its vertical plane is so high that it approximatively behaves as a rigid body, and vertical deflection at collapse are negligible. However, out-of-plane horizontal displacement of the free edge can result from the rigid rotation of the arch around the hinges at its footings, under the orthogonal horizontal thrust applied by the half-arches of the PG. The higher A_r , the higher the shear stiffness of the PG, the lower the amplitude of the boundary arch rigid body rotation outside its plan, the lower the resulting horizontal displacement at collapse. In the lower limit case of the unbraced structure ($A_{r,0}$), nil vertical displacements of the PG boundary involve LFs slightly higher than the ones of CG, whose buckling shape involves significant deflections along the central arch (See Fig. 9, first two columns, last two rows.) For low to moderate values of A_r , the not negligible shear deformability of the partial gridshell allows the arch to rigidly rotate out of its plane. It follows the LF of PG is always lower than the LF of CG. PG and CG LFs tend to the same value only for A_r upper limit value, where the extremely high shear stiffness of the PG does not allow significant rigid rotation of the boundary arch out of its plane. In other terms, free-edge displacements are almost nil both in the vertical and horizontal directions, and the same mode of instability occur for both PG and CG.

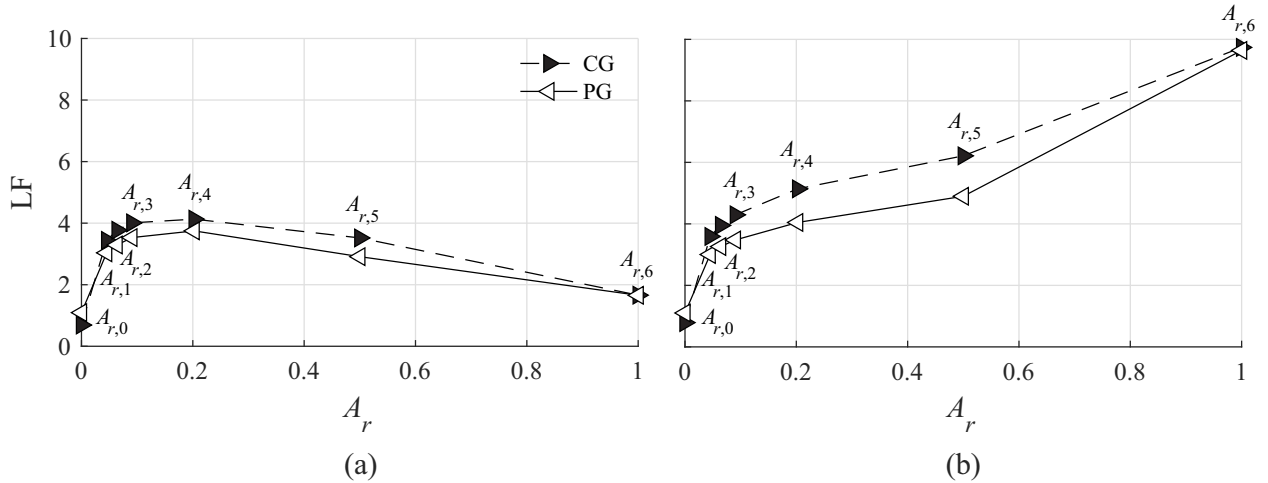


Figure 10: LF versus A_r ($I_r = 10^6$) for PG and CG with LBA(a) and GMNA (b)

In the next Section we propose a complementary, deeper insight of the results obtained by GMNA models. The analysis is focused on the PG with the values of A_r that are more relevant and recurrent in the design of bending-inactive hybrid single-layer free-edge gridshells ($A_{r,1}$, $A_{r,2}$, $A_{r,3}$, $A_{r,4}$). Therefore, the limit cases $A_{r,0}$, $A_{r,5}$ and $A_{r,6}$ are no longer considered.

6.2. Mechanical rephrasing

To comprehensively analyse the relative influence of the two design variables, the dimensionless ratio S_r is introduced:

$$S_r = \frac{I_r}{A_r}. \quad (10)$$

In words, such derived variable synthetically weights the flexural stiffness of the boundary arch to the shear stiffness of the braced gridshell. Figure 11 plots the LF versus S_r . This representation allows to recognise some common trends among the curves and related subranges of S_r , which were not clearly visible in Figure 8b. Specifically, three branches can be identified:

- for $S_r < 100$ the LF steeply increases for increasing S_r ;
- for about $100 < S_r < 400$ the LF trend changes with A_r , i.e. LF increases, remains constant or decreases for increasing value of A_r ;
- for $S_r > 400$ the LF moderately increases for increasing S_r . Moreover, for $S_r > 1000$ the curves have a common asymptotic trend.

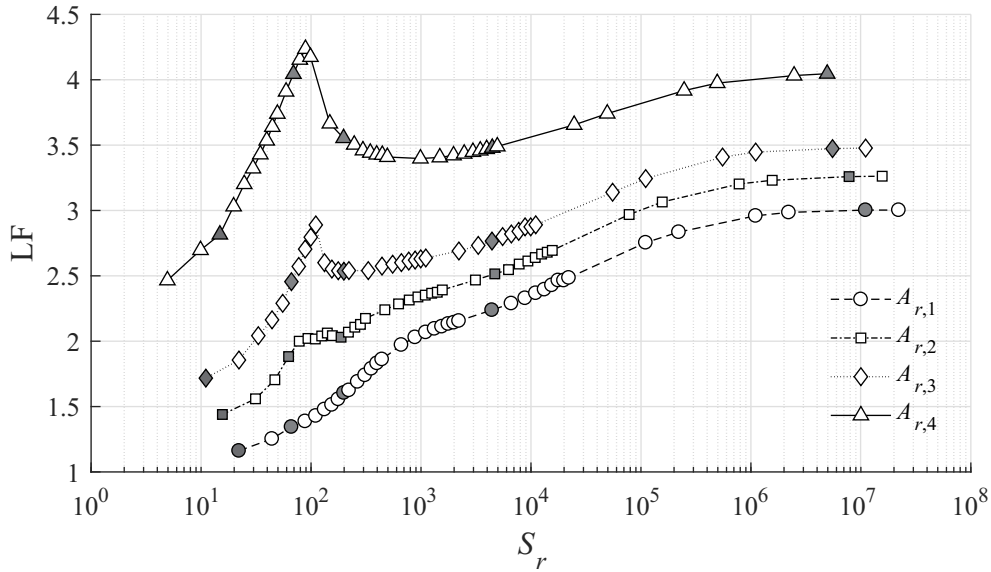


Figure 11: LF versus S_r for different values of A_r .

A deeper insight into the PG mechanical behaviour corresponding to the above identified S_r ranges is provided in Figures 12-13. They plot in plan, for representative values of S_r (see filled markers in Figure 11), the nodal observables at collapse ΔK and Γ introduced in Section 5, scaled with respect to their maximum values $\hat{\Delta K}$ and $\hat{\Gamma}$, respectively. The visualisation of these normalised nodal quantities allows to discuss the topology of the buckling shapes more precisely and clearly than classic magnified axonometric deformed shapes do, e.g. in Figure 9. In particular, both Figures highlight three recurrent instability modes that are common to all A_r values. For the sake of clarity and by way of example, recognised node patterns are qualitatively clustered by dashed contours in the $A_{r,2}$ rows:

- I. around low values of S_r (see first column), the highest deformations are concentrated along the boundary arch and adjacent nodes, and progressively diminish towards the spring line (red dashed contour);
- II. as S_r increases (see second column), the highest deformations involve the nodes adjacent to both the boundary arch and the outer ring;
- III. for high values of S_r (see third to fifth columns), the highest deformations are located in the nodes near the spring line (blue dashed contour), with a progressive involvement of a higher number of internal nodes as S_r increases.

In other words, when the boundary arch is relatively flexible, the collapse is *free-edge-driven* (I), i.e., it is mainly triggered by the buckling of the boundary arch. Conversely, when the boundary arch is relatively stiff, the collapse is *gridshell-driven* (III), that is, it is mainly initiated by the snap-through ring instability. In between, a transition mode (II) occurs, where both kind of instabilities are combined in the PG as a whole.

The spatial patterns briefly discussed above oriented us towards the heuristic definition of a further observable to identify more precisely the ranges of S_r in which the described instability modes take place:

$$\Gamma_r = \frac{\sum_{i=1}^{N_{\Omega_1}} \Gamma_i}{N_{\Omega_1}} \cdot \frac{N_{\Omega_2}}{\sum_{j=1}^{N_{\Omega_2}} \Gamma_j}, \quad (11)$$

where N_{Ω_1} and N_{Ω_2} are the number of nodes falling into the Ω_1 and Ω_2 regions, respectively (see scheme in Figure 14 on the right). In words, the defined observable is the ratio between the average in-plane nodal deformation in two regions selected a priori on the basis of the spatial patterns in Figures 12-13. This observable is intended to provide a bulk quantitative metric that synthetically describes the in-plane deformation patterns discussed above (Fig. 13). On the basis of the above equation, values of $\Gamma_r > 1$ describe the case where the in-plane deformations are mainly concentrated in the Ω_1 region (free-edge-driven deformation), while for $\Gamma_r < 1$ the deformations are mainly gridshell-driven. Figure 14 illustrates Γ_r versus S_r for the considered four values of A_r . The expected behaviour is generally confirmed and three main regimes corresponding to the above instability modes can now be clearly defined. Specifically:

- regime I corresponds to values of $\Gamma_r > 1$ for all three curves. Its upper bound $S_r = S_{r,I-II} \cong 50$ is given by the intersection between the $\Gamma_r = 1$ line and the $A_{r,2}$ curve;
- regime III corresponds to values of $\Gamma_r < 1$ for all three curves. Its lower bound $S_r = S_{r,II-III} \cong 120$ is given by the intersection between the $\Gamma_r = 1$ line and the $A_{r,3}$ curve;
- in between, a transition regime II is characterised by a sudden drop of Γ_r versus S_r . In this regime, different deformation patterns occur for different A_r values. In particular, in $A_{r,1}$ free-edge and shell-driven deformations are well balanced, in $A_{r,3}$ and $A_{r,4}$ the free-edge-driven deformation is more evident, while in $A_{r,2}$ the gridshell-driven behaviour prevails (compare Figure 13, second column). In other terms, the upper and lower bounds of regime II seem to depend on other parameters than S_r .

Moreover, regime III can be further divided into three sub-regimes on the basis of some common trends of the $\Gamma_r - S_r$ curves. In IIIa Γ_r varies non monotonically. Then, in IIIb, a monotonic decreasing trend can be recognised. Finally, in IIIc the three curves almost coincide and share a monotonic slightly increasing trend: in fact, as the arch stiffness tends to infinity, the collapse involves its out-of-plane rigid body rotation, which is retained by the gridshell in-plane shear stiffness. Therefore, an increasingly higher number of nodes in the Ω_1 region is involved in the deformation (see Fig. 13, third to fifth columns and related comments).

It can be observed that the general trend of $\Gamma_r(S_r)$ in Figure 14 and the features of the recognised regimes recall other transitional physical phenomena, such as the evolution of the mean drag aerodynamic coefficient with Reynolds number for a circular cylinder (compare [71], Fig. 4.5.2, and [72], Fig. 7.28).

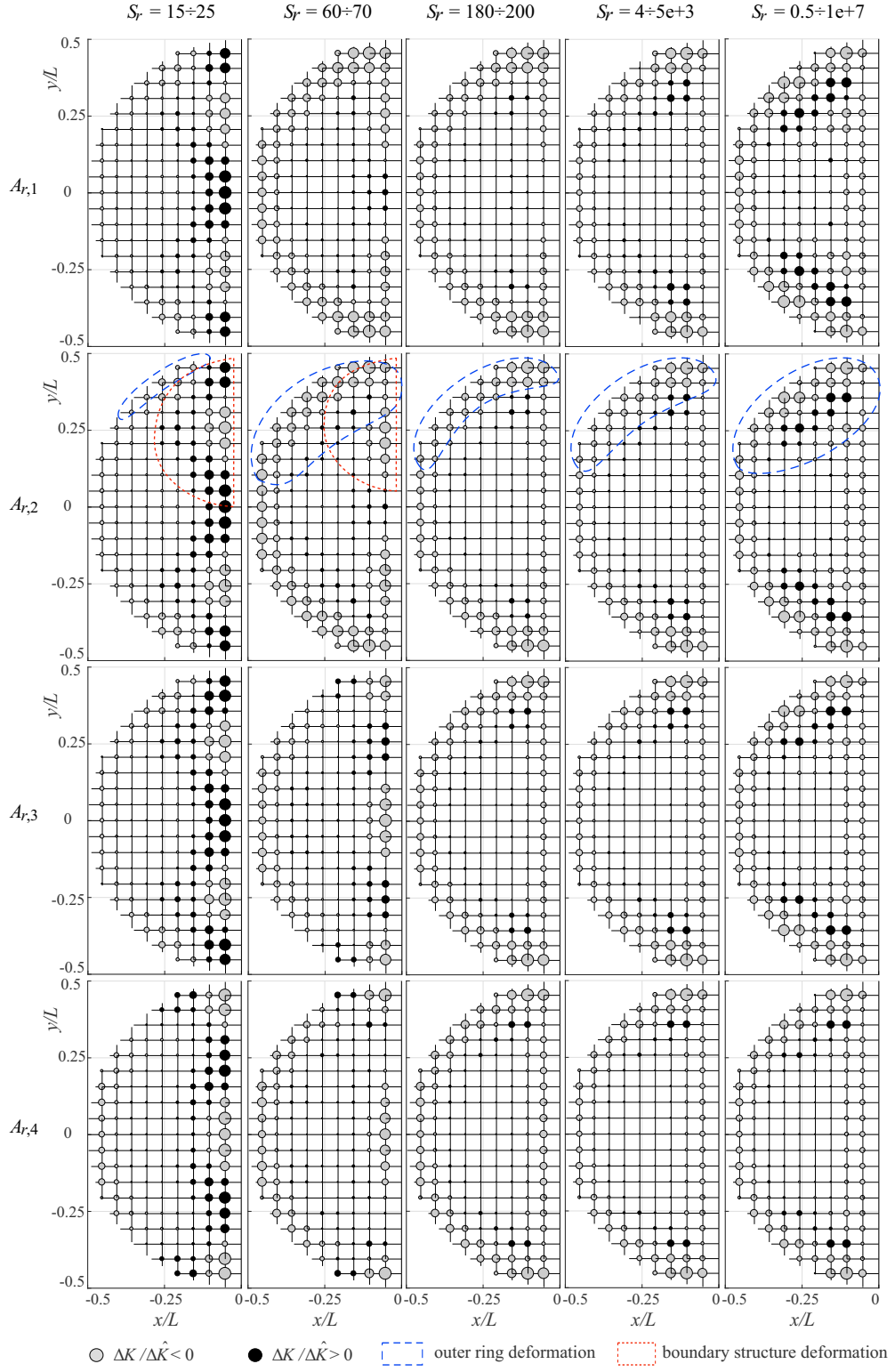


Figure 12: $\Delta K / \hat{\Delta K}$ for different S_r and A_r

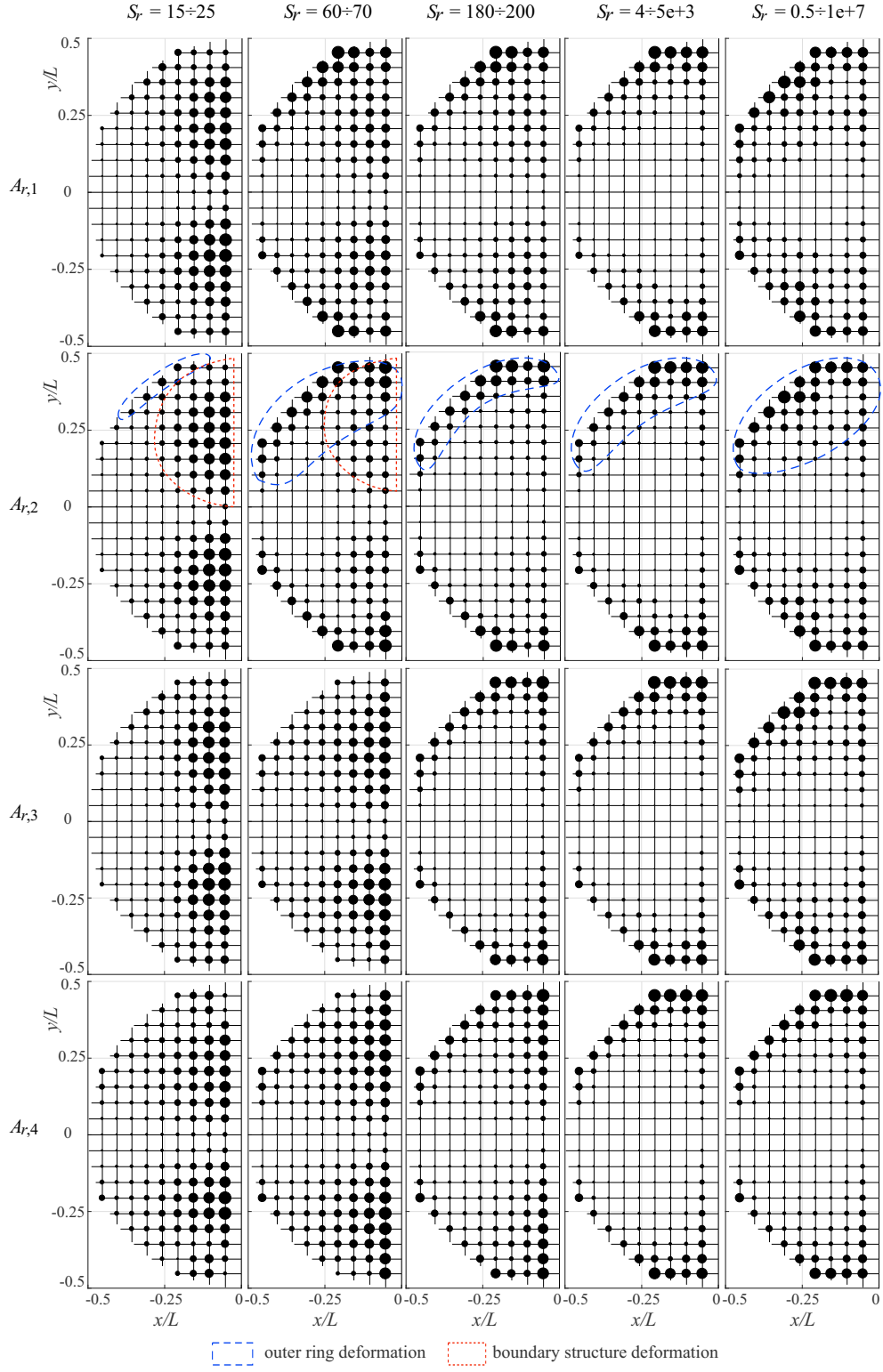


Figure 13: $\Gamma/\hat{\Gamma}$ for different S_r and A_r

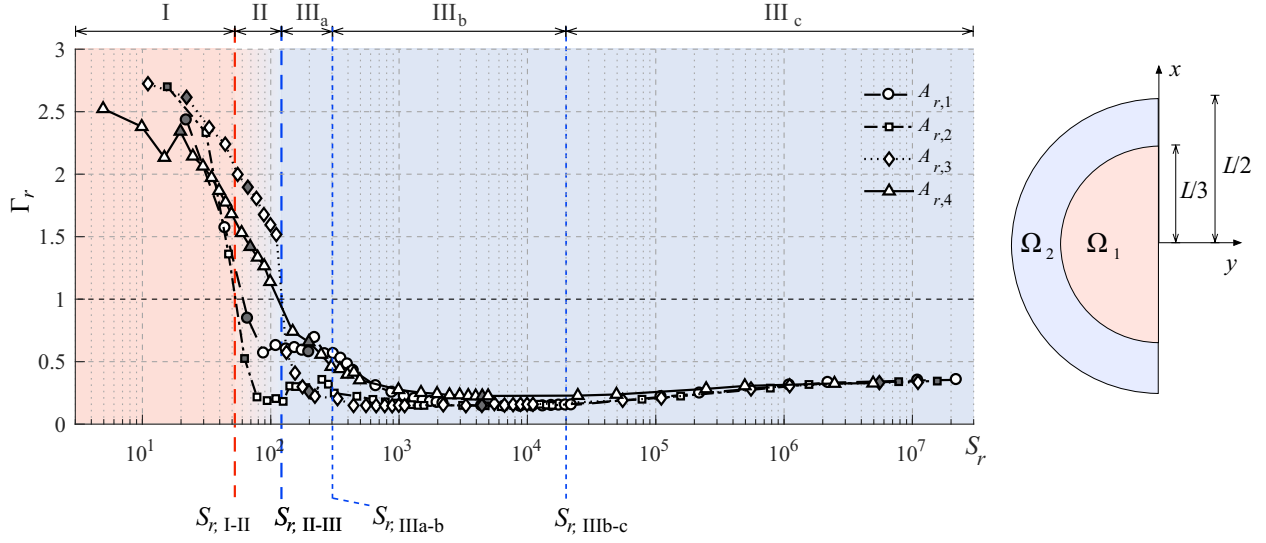


Figure 14: Γ_r versus S_r for different A_r (filled markers highlights the cases analysed in Figures 12 and 13)

6.3. Range-finding chart

On the basis of the analysis illustrated in the previous sub-Sections, a range-finding chart within the design parameter space is proposed in the following. The aim of the chart is to orient the structural analyst in identifying the preferred regime and, hence, possible ranges of the design parameters I_r and A_r .

The chart in Figure 15 plots the $I_r - A_r$ couples, which satisfy the following expression, obtained by substitution of Eq.s (1) in Eq. (10):

$$I_r = S_r A_r. \quad (12)$$

The straight lines delimiting the regime boundaries are obtained by substituting in Eq. (12) the values of S_r corresponding to the regime boundaries (see Fig. 14). In the chart, the design parameter space is limited to low values of both I_r and A_r in order to focus on the values of practical interest for bending-inactive hybrid single-layer steel gridshells. The $I_r - A_r$ couples of the built gridshells collected in Figure 3 are included for reference (black squares). It can be observed that the latter ones lie in Regime IIIb: this seems to prove that skilled designers size both grid and boundary structural elements such as to avoid boundary-driven instability (regimes I and II) and, in general, the regimes characterised by the high variability of LF.

Note that the chart in Figure 15 has been determined for the specific PG analysed in this study and can not therefore be considered as generally valid from a quantitative point of view. Nevertheless, the qualitative trend reported in the chart is expected to hold also for different gridshell set-ups.

7. Conclusions

The present study was conducted to define, classify and analyse, from a mechanical point of view, a specific kind of gridshell structures, here named “Partial Gridshell” as opposed to “Complete Gridshells”. PGs are gridshells whose form is delimited by two or more geometrical cuts. The intersections between the gridshell and the delimitation surfaces give rise to a spring line - along which the PG is rigidly constrained - and one or more curved free-edges. Despite the prevailing occurrence of this gridshell type in the building practice, the studies that systematically discuss the stability of gridshell domes always adopt CGs with horizontal spring lines as benchmarks.

An ideal hybrid PG is adopted as a benchmark to investigate its local and global stability. In particular, its sensitivity to the flexural stiffness of the boundary structure and to the shear stiffness of the gridshell are investigated through an extensive parametric analysis by numerical experiments. The adopted parameters are the ratio of the boundary arch and grid element moment of inertia I_r , and the ratio of the bracing cable and grid element cross section

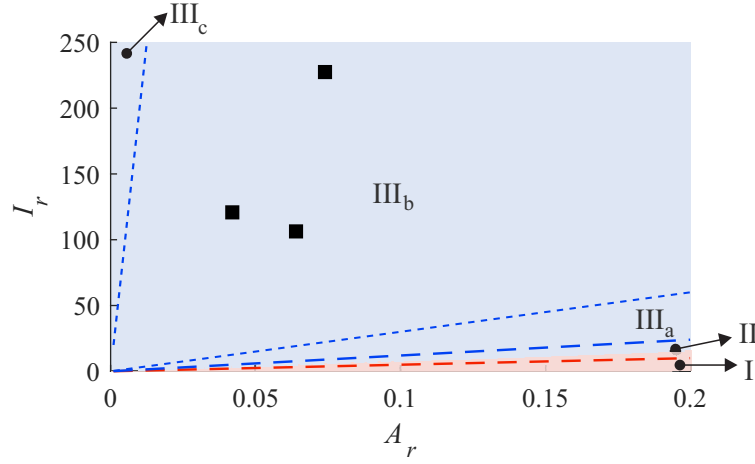


Figure 15: Range-finding chart in the I_r - A_r design plan

area A_r . The load factor and the collapse deformed shape under a uniform loading scenario are determined through geometrically and materially non-linear analysis.

The analysis of the results have highlighted the existence of three different mechanical regimes, depending on the value of the dimensionless parameter S_r . The latter was defined to evaluate the relative influence of the two design parameters I_r and A_r on the stability of the PG. Specifically:

- regime I ($S_r \approx < 50$) is characterised by a free-edge-driven collapse, i.e., in-plane and out-of-plane deformations mainly involve the boundary arch and adjacent gridshell nodes;
- regime II ($50 \approx < S_r \approx < 120$) shows a combined behaviour, where both free-edge-driven and gridshell-driven instabilities occur;
- regime III ($S_r \approx > 120$) is characterised by a shell-driven collapse, where the main in-plane and out-of-plane deformations mostly involve the gridshell nodes in the outer ring adjacent to the spring line.

Finally, a range-finding chart in the design parameter plan is proposed as a qualitative tool for designers to identify the preferred regime and associated values of the design parameters. Remarkably, the built bending-inactive hybrid single-layer steel gridshells reviewed in the present survey lie in Regime IIIb: this seems to prove that skilled designers size both grid and boundary structural elements such as to avoid free-edge-driven instability (regimes I and II).

These results, despite relative to a specific geometrical and structural set-up, contribute to shed some light on the behaviour of bending-inactive free-edge gridshell structures. Although gridshell geometry, free-edge geometry and their stiffness greatly vary in design practice, the overall results of this study are likely to be general at least in a qualitative sense. In other words, the mechanical interaction between out-of-plane boundary stiffness and in-plane gridshell stiffness is expected to take place as a rule, and regimes I and III are likely to occur in general. Conversely, the watershed values of S_r at which transition between regimes occurs and the transition mode (including their combination in regime II) are expected to strongly depend on the specific features of each structure. For instance, subsequent studies could be devoted to the effect of geometrical factors, i.e. the kind and orientation of the trimming surface with respect to the grid direction, the ratio between the gridshell and free-edge span, and to the joint effects of imperfections. The generalisation of the study to bending-active gridshells is not straightforward and requires further investigations, in the wake of the few comparative studies between bending-active and inactive gridshells (e.g. [73]), and the preliminary evaluation of the free-edge role in the stability of bending-active gridshells [74].

Acknowledgements

The authors would like to thank Vittorio Nascé, Emeritus Professor at Department of Architecture and Design, Politecnico di Torino, for the fruitful discussions about the paper topics and challenges.

References

- [1] M. Beckh, R. Barthel, The first doubly curved gridshell structure - Shukhovs building for the plate rolling workshop in Vyksa, in: *Proceedings of the Third International Congress on Construction History*, Cottbus, 2009.
- [2] R. Fuller, J. Ward, The artifacts of R. Buckminster Fuller: a comprehensive collection of his designs and drawings, Garland, 1985.
- [3] I. Liddell, Frei otto and the development of gridshells, *Case Studies in Structural Engineering* 4 (2015) 39–49.
- [4] J. Schlaich, H. Schober, Glass-covered grid-shells, *Structural Engineering International* 6 (2) (1996) 88–90.
- [5] H. Schober, *Transparent Shells: Form, Topology, Structure*, John Wiley & Sons, 2015.
- [6] F. Otto, E. Shauer, J. Hennicke, IL 10 Gitterschalen / Grid Shells, Stuttgart, 1974.
- [7] B. Burkhardt, O. Frei, IL 13 Multihalle Mannheim, Stuttgart, 1978.
- [8] A. Holgate, Glass Grid Roofs. The Art of Structural Engineering: The Work of Jörg Schlaich and His Team, 1997.
- [9] J. Chilton, G. Tang, *Timber Gridshells: architecture, structure and craft*, Routledge, 2017.
- [10] L. du Peloux, F. Tayeb, O. Baverel, J. Caron, Construction of a large composite gridshell structure: A lightweight structure made with pultruded glass fibre reinforced polymer tubes, *Structural Engineering International* 26 (2) (2016) 160–167.
- [11] D. Rockwood, *Bamboo Gridshells*, 2015.
- [12] P. Davey, *Engineering for a Finite Planet: Sustainable solutions by Buro Happold*, 2009.
- [13] V. Gioncu, Buckling of reticulated shells: State-of-the-art, *International Journal of Space Structures* 10 (1) (1995) 1–46.
- [14] K. Ishikawa, S. Kato, Elastic-plastic dynamic buckling analysis of reticular domes subjected to earthquake motion, *International Journal of Space Structures* 12 (3–4) (1997) 205–215.
- [15] S. Kato, M. Fujimoto, T. Ogawa, Buckling load of steel single-layer reticulated domes of circular plan, *Journal of the International Association for Shell and Spatial Structures* 46 (147) (2005) 41–63.
- [16] A. López, I. i. Puente, M. A. Serna, Direct evaluation of the buckling loads of semi-rigidly jointed single-layer latticed domes under symmetric loading, *Engineering Structures* 29 (2007) 101–109.
- [17] S. Yamada, Buckling load evaluation method for single layer cylindrical lattice shells, *Journal of Civil Engineering and Architecture* 6 (3) (2012) 268–279.
- [18] F. Fan, J. Yan, Z. Cao, Stability of reticulated shells considering member buckling, *Journal of Constructional Steel Research* 77 (2012) 32–42.
- [19] J. Cai, L. Gu, Y. Xu, J. Feng, J. Zhang, Nonlinear stability analysis of hybrid grid shells, *International Journal of Structural Stability and Dynamics* 13 (1) (2013) 1–16.
- [20] J. Yan, F. Qin, Z. Cao, F. Fan, Y. Mo, Mechanism of coupled instability of single-layer reticulated domes, *Engineering Structures* 114 (2016) 158–170.
- [21] D. Wright, Membrane forces and buckling in reticulated shells, *Journal of the Structural Division, ASCE* 91 (1965) 173–201.
- [22] K. Heki, The continuum treatment of discrete systems and its application to the analysis of lattice structures, *Bulletin of the IASS XXVI-3* (89) (1985) 17–24.
- [23] S. J., General stability analysis of lattice shells by continuum modeling, *International Journal of Space Structures* 7 (4) (1992) 275–284.
- [24] S. Malek, T. Wierzbicki, J. Ochsendorf, Buckling of spherical cap gridshells: A numerical and analytical study revisiting the concept of the equivalent continuum, *Engineering Structures* 75 (15) (2014) 288–298.
- [25] D. Tonelli, N. Pietroni, E. Puppo, M. Froli, P. Cignoni, G. Amendola, R. Scopigno, Stability of statics aware Voronoi grid-shells, *Engineering Structures* 116 (2016) 70–82.
- [26] T. Bulenda, J. Knippers, Stability of grid shells, *Computer & Structures* 79 (2001) 1161–1174.
- [27] F. Fan, Z. Cao, S. Shen, Elasto-plastic stability of single-layer reticulated shells, *Thin-Walled Structures* 48 (2010) 827–836.
- [28] C. Borri, P. Spinelli, Buckling and post-buckling behavior of reticulated shells affected by random imperfections, *Computer & Structures* 30 (4) (1988) 937–943.
- [29] S. Kato, I. Mutoh, M. Shomura, Collapse of semi-rigidly jointed reticulated domes with initial geometric imperfections, *Journal Constructional Steel Research* 48 (1998) 145–168.
- [30] S. Yamada, A. Takeuchi, Y. Tada, K. Tsutsumi, Imperfection-sensitive overall buckling of single-layer lattice domes, *Journal of Engineering Mechanics* 127 (2001) 382–386.
- [31] A. Zhang, X. Zhang, J. Ge, Influence of initial geometrical imperfections on stability of a suspendome for Badminton Arena for 2008 Olympic Games, *Spatial Structures* 12 (4) (2006) 8–12, in Chinese.
- [32] J. Guo, Research on distribution and magnitude of initial geometrical imperfection affecting stability of suspen-dome, *Advanced Steel Construction* 7 (4) (2011) 344–358.
- [33] F. Fathelbab, The effect of joints on the stability of shallow single layer lattice domes, Ph.D. thesis, University of Cambridge (1987).
- [34] K.-J. Hwang, J. Knippers, S.-W. Park, Influence of various types node connectors on the buckling loads of grid shells, in: *IASS Symposium*, 2009.
- [35] H. Ma, F. Fan, P. Wen, H. Zhang, S. Shen, Experimental and numerical studies on a single-layer cylindrical reticulated shell with semi-rigid joints, *Thin-Walled Structures* 86 (2015) 19.
- [36] F. Fan, J. Yan, Z. Cao, Elasto-plastic stability of single-layer reticulated domes with initial curvature of members, *Thin-Walled Structures* 60 (2012) 239–246.
- [37] J. Cai, Y. Xu, J. Feng, J. Zhang, Nonlinear stability of a single-layer hybrid grid shell, *Journal of Civil Engineering and Management* 18 (5).
- [38] L. Bruno, M. Sassone, F. Venuti, Effects of the equivalent geometric nodal imperfections on the stability of single layer grid shells, *Engineering Structures* 12 (2016) 184–199.
- [39] R. Mesnil, C. Douthe, O. Baverel, B. Léger, Linear buckling of quadrangular and kagome gridshells: A comparative assessment, *Engineering Structures* 132 (2017) 337–348.
- [40] T. Ueki, S. Kato, I. Kubodera, Y. Mukaiyama, Study on the elastic and elasto-plastic buckling behaviour of single layered domes composed of members having axial and bending springs at the ends, in: *IASS Symposium*, 1991.

- [41] S. Kato, S. Yamada, H. Takashima, R. Shibata, Buckling stress of a member in a rigidly jointed single-layer reticular dome, in: IASS Symposium, 1991.
- [42] I. for Metal Spatial Structures, (Draft) Guide to buckling load evaluation of metal reticulated roof structures, Tech. rep., International Association for Shell and Spatial Structures (2014).
- [43] J. Schlaich, H. Schober, Glass roof for the Hippo House at the Berlin Zoo, *Structural Engineering International* 7 (4) (1997) 252–254.
- [44] J. Abel, J. Chilton, Heinz isler - 50 years of "new shapes for shells", *Journal of the International Association for Shell and Spatial Structures* 52 (3).
- [45] M. Garlock, D. Billington, Felix Candela: Engineer, Builder, Structural Artist, Yale University Press, 2008.
- [46] L. Kollár, E. Dulácska, Buckling of shells for engineers, Wiley, Chichester, 1984.
- [47] S. Timoshenko, J. Gere, Theory of elastic stability, McGraw Hill, New York, 1961.
- [48] L. Donnell, Beams, plates and shells, McGraw-Hill, New York, 1976.
- [49] W. Flugge, Stress in shells, Springer-Verlag, Berlin, 1960.
- [50] A. Zingoni, Liquid-containment shells of revolution: A review of recent studies on strength, stability and dynamics, *Thin-Walled Structures* 87 (2015) 102–114.
- [51] L. Godoy, Buckling of vertical oil storage steel tanks: Review of static buckling studies, *Thin-Walled Structures* 103 (2016) 1–21.
- [52] C. Douthe, O. Baverel, J. Caron, Gridshell in composite materials: towards wide span shelters, *Journal of the International Association for Shell and Spatial Structures* 48 (3) (2007) 175–180.
- [53] M. Kahl, T. Mansperger, Überdachung des kleinen Schlosshofes des Residenzschlosses Dresden, *Stahlbau* 82 (7) (2013) 531–536.
- [54] C. Williams, The analytical and numerical definition of the geometry of the British Museum Great Court roof, in: *Mathematics and Design* 2001, 2001.
- [55] E. Happold, W. Liddell, Timber lattice roof for the Mannheim Bundesgartenschau, *The Structural Engineer* 53 (3) (1975) 99–135.
- [56] C. Poirriez, T. Wortmann, R. Hudson, Y. Bouzida, From complex shape to simple construction: fast track design of the "Future of us gridshell" in Singapore, in: T. T. K. Kawaguchi, M. Ohsaki (Ed.), *Proceedings of the IASS Annual Symposium 2016 Spatial Structures in the 21st Century*, 2016.
- [57] J. Glymph, D. Shelden, C. Ceccato, J. Mussel, H. Schober, A parametric strategy for free-form glass structures using quadrilateral planar facets, *Automation in Construction* 13 (2) (2004) 187–202.
- [58] H. Schober, S. Justi, Cabot Circus, Bristol - Ebene Vierecknetze für freigeformte glasdächer, *Stahlbau* 81 (Supplement S1) (2012) 28–42.
- [59] A. Pena de Leon, Two case-studies of freeform-facade rationalization, in: *Proceedings of the 30th International Conference on Education and research in Computer Aided Architectural Design in Europe*, Vol. Modes of Production - Volume 2, 2012, pp. 491–500.
- [60] Toledo gridshell, http://www.gridshell.it/gridshell_napoli/.
- [61] A. Cattnach, Waitomo Caves Visitor Centre, New Zeland Timber Design Journal 18 (3) (2010) 7–12.
- [62] O. Kelly, R. Harris, M. Dickson, The construction of the Downland gridshell, *The Structural Engineer* 79 (17) (2005) 25–33.
- [63] R. Harris, S. Haskins, J. Roynon, The Savill Garden gridshell: design and construction, *The Structural Engineer* 86 (17) (2008) 27–34.
- [64] SCI Steel Knowledge, Schubert Club Band, Structural Stainless Steel Case Study 10 (2012) 1–4.
- [65] G. Del Guerra, M. Froli, Proposal to roof the courtyards of an historical building in Pisa with glass and steel grid shells: Form finding and stability problems, *Journal of Architectural Engineering ASCE* 15 (2) (2009) 62–66.
- [66] B. D'Amico, A. Kermani, H. Zhang, A. Pugnale, S. Colabella, S. Pone, Timber gridshell: numerical simulation, design and construction of a full scale structure, *Structures* 3 (2015) 227–235.
- [67] Eurocode 3 UNI EN 1993-1-6:2007: Eurocode 3: Design of steel structures - Part 1-6: Strength and stability of shell structures (2007 2004).
- [68] SAS IP, Inc., ANSYS, Inc. Theory Manual. (2011).
- [69] C. R. Calladine, Theory of Shell Structures, 1983.
- [70] L. Najman, P. Romon, Modern approaches to discrete curvature, Springer International Publishing, 2017.
- [71] E. Simiu, R. Scanlan, Wind Effects on Structures: Fundamentals and Applications to Design, John Wiley & Sons Inc, 1996.
- [72] Eurocode 1 UNI EN 1991-1-4:2005: Actions on structures - Part 1-4: General actions - Wind actions.
- [73] S. Kato, M. Fujimoto, T. Ogawa, Reliability analysis of buckling of reticulated single layer roofs of general form under vertical loads, *Journal of the International Association for Shell and Spatial Structures* 57 (3) (2016) 227–244.
- [74] F. Tayeb, J.-F. Caron, O. Baverel, L. D. Peloux, Stability and robustness of a 300m² composite gridshell structure, *Construction and Building Materials* 49 (2013) 926–938.